Dalton Transactions

ROYAL SOCIETY OF CHEMISTRY

PAPER

View Article Online
View Journal | View Issue



Check for updates

Cite this: *Dalton Trans.*, 2023, **52**, 11965

# Electronic and electrocatalytic properties of $PbTiO_3$: unveiling the effect of strain and oxygen vacancy†

L. Bendaoudi,[a] T. Ouahrani, *[b,c] A. Daouli, [d] B. Rerbal, [a] R. M. Boufatah, [c] Á. Morales-García, [e] R. Franco,[f] Z. Bedrane,[c] M. Badawi [d] and D. Errandonea *[g]

Received 17th May 2023,
Accepted 2nd August 2023

DOI: 10.1039/d3dt01478a

rsc.li/dalton

First-principles calculations based on density-functional theory have been used to investigate the effect of biaxial strain and oxygen vacancy on the electronic, photocatalytic, and electrocatalytic properties of $PbTiO_3$ oxide. Our results show that $PbTiO_3$ has a high exciton binding energy and a band gap that can be easily moderated with different strain regimes. From a reactivity viewpoint, the highly exothermic adsorption of hydrogen atoms in both pristine and strained $PbTiO_3$ structures does not make it a potential electrocatalyst for the hydrogen evolution reaction. Fortunately, the presence of oxygen vacancies on the $PbTiO_3$ surface induces moderate adsorption energies, making the reduced $PbTiO_3$ suitable for hydrogen evolution reaction processes.

## 1 Introduction

The current energy crisis has put on the table the urgency to find and use alternative energy resources utilizing sustainable and clean solar energy. Photovoltaic, water splitting, and photothermal methods could be some of the solutions. However, all of them need appropriate materials with suitable electronic and optical properties. For photocatalytic (PV) applications, for instance, to have the capacity to harvest solar energy, the material should have a high light absorption ($\sim 10^5$ $cm^{-1}$ for >1.4 eV).[1,2] A low carrier recombination loss and efficient carrier collection efficiency are also prerequisites, as well as a long optical path, to promote photon recycling.[3] On the other hand, to be used as a photocatalyst (PC),[4] the material should achieve reasonable reaction rates, generate charge carriers, and guarantee the surface sites for hole-mediated oxidation or electron-mediated reduction. For both applications, the semiconductor should also be abundant, which limits the range of PV/PC materials. This fact, however, could be overcome if the properties of the material were modulated. In semiconductor production, doping is one of the most feasible methods to modulate its electronic properties.[5] The electronic band gap can be increased by anion or cation substitution; however, this method is not easy to control[6] because many reactions could happen due to low solubility. Atomic substitutions can also create inappropriate structural distortions of the material,[7] making it unsuitable for PC applications. To modulate a PC material, an electric field, and a strain-induced band-gap could also be efficiently used.[8,9]

Ferroelectric materials have recently attracted a lot of attention in research due to their use in solar conversion as well as photocatalyst materials for water splitting to produce $H_2$, or for $CO_2$ reduction. These materials allow the external control of the internal electric fields and injection barriers, which lie at the heart of the PC mechanism.[3] Sandwiched between electrodes, their properties can be modified by sun-light-generated photo-excited charge carriers, which activate a polarization-induced internal electric field. This field helps to separate the photo-excited charges (electrons and holes), due to Schottky barriers,[10] which deplete the ferroelectric layers. This also

[a]*Laboratory of Materials Discovery, Unit of Research Materials and Renewable Energies, LEPM-URMER, Université de Tlemcen 13000, Algeria*
[b]*École supérieure en sciences appliquées, ESSA-Tlemcen, BB 165 RP Bel Horizon, Tlemcen 13000, Algeria. E-mail: tarik_ouahrani@yahoo.fr*
[c]*Laboratoire de Physique Théorique, Université de Tlemcen, BP 119, 13000, Algeria. E-mail: tarik_ouahrani@yahoo.fr*
[d]*Université de Lorraine and CNRS, LPCT, UMR 7019, 54506 Vandoeuvre-lés-Nancy, France*
[e]*Departament de Ciéncia de Materials i Química Física & Institut de Química Teórica i Computacional (IQTCUB), Universitat de Barcelona, c/Martí i Franquès 1-11, 08028 Barcelona, Spain*
[f]*(MALTA) Consolider Team and Departamento de Química Física y Analítica, Universidad de Oviedo, E-33006 Oviedo, Spain*
[g]*Departamento de Física Aplicada - Instituto de Ciencia de Materiales, Matter at High Pressure (MALTA) Consolider Team, Universidad de Valencia, Edificio de Investigación, C/Dr. Moliner 50, Burjassot, 46100 Valencia, Spain. E-mail: daniel.errandonea@uv.es*

† Electronic supplementary information (ESI) available. See DOI: https://doi.org/10.1039/d3dt01478a

induces opposite transport directions of positive and negative charges in the electric field, making ferroelectric materials candidates for light absorbers and photocatalysts with the potential capacity to realize directed separation of photogenerated electron–hole pairs. The most interesting ferroelectric materials crystallize in a perovskite-type structure, such as $BaTiO_3$,[11] $PbTiO_3$,[12] and $BiFeO_3$.[13] $PbTiO_3$ at ambient conditions has a tetragonal crystal structure described by space group *P4mm* ($C_{4v}$).[14–16] It is represented in Fig. 1. It has been shown that in $PbTIO_3$ ferroelectric polarization can activate the photocatalytic activity.[17] The ferroelectricity in $PbTiO_3$ is generated by spontaneous dipole moments originating from the displacements of Pb and Ti atoms in opposite directions to the typical positions of a perovskite. As a consequence, the $TiO_6$ octahedron is highly distorted inducing a crystal polarization.

So far, many ferroelectric semiconductors and their composites have been investigated for their interesting optical properties. They are considered as promising candidates for light-absorbing materials for applications in solar energy conversion devices. Nevertheless, they exhibit a wide band gap (3–5 eV). So the domain of light absorption is restrained in the ultraviolet (UV) region, so, they have a low efficiency.[18] Since UV light comprises only 8% of the solar spectrum, new materials with a smaller band gap and large polarization would be highly desirable. $PbTiO_3$ could be one of the most promising electrocatalytic materials. It has also been widely used to fabricate various microelectronic and optoelectronic devices, including non-volatile ferroelectric random access memories, microsensors, microactuators, integrated capacitors, and electro-optic modulators.[19] However, there are some concerns about the use of $PbTiO_3$ for applications because of the potential toxicity of lead oxides. But these concerns have been resolved in a recent study where it was shown that potential toxicity could be avoided by adding a transparent phosphate salt ($NH_4HPO_4$) to the devices.[20] The salt will react with the lead, forming a highly insoluble compound, without alternating the advantageous optoelectronic properties of $PbTiO_3$. As a consequence, several theoretical and experimental studies have been carried out on this material. Xue *et al.*[21] investigated two-dimensional (2D) $PbTiO_3$ films and discovered that surface modification modeling its ferroelectric and polarisable properties allows for functionalization. Its optical properties were also tuned by doping with copper doping[22] or with rare-earth elements.[23] ZnO $(12\bar{1}0)$/$PbTiO_3$ (001) heterostructures, band alignments, and polarization properties were studied.[24] Lattice distortions,[25] thermal expansion,[26] and vibrational properties were studied[27,28] for bulk and thin layers.[29,30] Despite enormous efforts to study the electronic properties of $PbTiO_3$, its photo/electrocatalytic properties are still in their early stages, and the resulting effects are less explored. Additionally, most of these studies focus on its cubic structure, rather than its stable tetragonal structure.

Another relevant fact for photoelectric applications is the exciton-binding energy ($E_b$) coming from the bound of electron–hole pairs. Low $E_b$ semiconductors are more prone to spontaneous exciton dissociation and are therefore preferred for photovoltaic applications such as solar cells.[31] In particular, effective exciton accumulation is an essential precondition for gaining advanced energy-transfer-initiated photocatalysis. This is because excitons can serve as photoinducedspecies that dominate photoexcitation properties involving energy transfer, opening up an alternative pathway for realizing versatile photocatalytic solar-energy conversion.[32] In particular, high $E_b$, interfacial energy level offsets are required to drive exciton dissociation into free charge carriers at the donor/acceptor interfaces, resulting in an extra energy loss. A high $E_b$ can also improve charge generation yields and thus photocatalytic activities.[17] Our interest in this paper is to study how to improve the electronic properties and excitonic binding effect in tetragonal $PbTiO_3$. Tuning the value of the electronic band gap can be a critical step in incorporating a charge-carrier-involved photocatalytic reaction. We will use lattice strain/single oxygen vacancy site as a route to control the band-gap energy.[33]

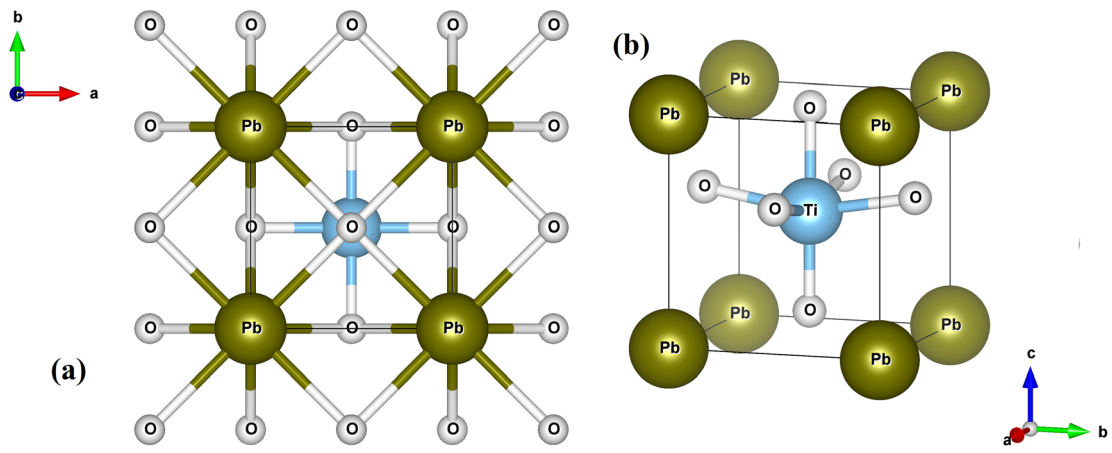


**Fig. 1** The crystal structure of the tetragonal phase of $PbTiO_3$. Dark green, light blue, and white spheres represent Pb, Ti, and O atoms. (a) (001) projection showing Pb–O and Sn–O bonds. (b) Perspective showing the $TiO_6$ distorted octahedron.

Computer simulations based on density-functional theory are an efficient tool for studying the influence of lattice strain, defects, heteroatoms, doping, and surface/interface building on the photocatalytic performance of materials.[34–40] Using this method, Zhao *et al.*[41] demonstrated that the application of tensile strains could improve the hydrogen evolution reaction (HER) activity of an h-$B_2O$ monolayer to reach low hydrogen coverage. Knowing that the polarization in the (110) slab is more significant than that of the (001) slab,[42] we have chosen to analyze the second one. This choice has been made in order to minimize the effect of polarization and favor only analyzing the role of strains or the single oxygen vacancy in the photocatalytic properties of $PbTiO_3$. In addition, the $PbTiO_3$ (001) surface includes two neutral planes, PbO and $TiO_2$, which respective surface energies are 0.717 and 0.633 J $m^{-2}$. In contrast, the $PbTiO_3$ (110) surface consists of two charged planes, $O_2$ and $PbTiO_3$ (with surface energies of 2.747 and 2.357 J $m^{-2}$). Therefore, both terminations of the (001) surface are more stable than those of the (110) surface in view of energy minimization.[43] Thus, as bottlenecks of catalytic application, we will briefly analyze how hydrogen reacts with the surface of pristine, defective, and strained slabs of $PbTiO_3$. For this task, we will use two slabs, the first is a $PbTiO_3$(001)-(2 × 2) $TiO_2$-terminated and the second as $PbTiO_3$(001)-(2 × 2) PbO-terminated. The latter has the lowest surface energy among all possible cleavages including higher-index planes. Attempts were already made to analyze HER on $PbTiO_3$, but they were focused on the effects of oxygen vacancy ($O_v$)[44] or ferroelectric polarization.[17] The use of oxygen vacancy ($V_O$) demonstrated its efficacy for active sites for reaction participation, which improves light harvesting and charge carrier concentration with better charge separation. Notably, it was shown that without the use of $V_O$, it is thermodynamically difficult to dissociate H atoms from water molecules.[44] This dissociation is mandatory to get $H_2$ molecules. This conclusion was also elucidated from experiments.[17] In this paper, we aim to see the influence of both strain and the vacancy sites $V_O$ on the surface of $PbTiO_3$ on its electrocatalytic properties (see the ESI† for the study of defect $V_O$ structure). We have analyzed the HER activity and decided which is the more favorable route to activate the sites of $PbTiO_3$. In this way, we can analyze which configuration can provide the necessary energy to hold hydrogen species in place on the surface of $PbTiO_3$ material. The second part of the paper deals with the calculation of the excitonic binding energy essential.

## 2 Computational details

This work analyzes tetragonal bulk lead titanate $PbTiO_3$ and a slab geometry with (001) surface normal and polarization axis. To isolate periodic slabs, we introduced a vacuum of 15 Å. A dipole correction in the center of the vacuum is also used in order to get rid of the artificial electrical field and the non-physical dipole–dipole interactions among slabs in the $z$ direction. Calculations were based on density-functional theory (DFT)[45] and implemented with the Vienna *ab initio* simulation code (VASP).[46] VASP provides a suite of tools and algorithms to solve the Kohn–Sham equations, which describe the quantum mechanical behavior of electrons in a solid. We used a DFT-D3 approach including a Becke–Jonhson damping[47,48] simulating the dispersion corrections of Grimme. The interactions between the valence and the frozen core electrons were simulated with the projector augmented wave (PAW) method,[49] and electron exchange and correlations were treated within the generalized-gradient approximation (GGA).[50] The occupation of Kohn–Sham orbitals was smeared with a 0.1 eV width according to the first-order Methfessel–Paxton scheme.[51] The structures were first subject to optimization for forces lower than 0.005 eV $Å^{-1}$. Plane-wave basis sets with a kinetic energy cutoff of 520 eV were used. The orbitals are sampled as regular 12 × 12 × 11 mesh centered at Γ point of the Brillouin zone.

In order to counteract the problems associated with the DFT-self-interaction error, which can artificially delocalize the on-site coulombic interactions of d- in the Ti atoms and oxygen 2p subspaces in $PbTiO_3$ affecting both structural and electronic properties,[52] a GGA+$U$ methodology was employed.[53] For our non-magnetic oxide compounds, the Hubbard correction ($U_{eff} = U - J$) was tested and converged for $U$ = 6 eV for Ti 3d, $U$ = 2 eV for O 2p states and $J$ = 2 eV (see Fig. S1 the ESI†). Where $U$ and $J$ correspond respectively to Hubbard and Hund's corrections.[53] The band structures were calculated by and GGA+$U$ approach. The phonon dispersion calculations were achieved usingthe supercell method[54] and were integrated into the free software Phonopy.[55] Mechanical properties were calculated using the stress–strain analysis methodology developed in the VaspKit toolkit[56] integrated with the VASP code. To investigate the effect of strains and defect[57] single oxygen vacancy on tetragonal $PbTiO_3$, a biaxial compression regime was selected. This regime has been recently reported as one of the most efficient ways to modulate the electronic character of most materials. A strain ($\sigma$) condition was utilized as $\sigma_{xy} = \frac{a - a_0}{a_0}$ where $a_0$ and $a$ correspond to equilibrium and strained lattice values,[58] respectively.

To estimate the exciton binding effect, we used a many-body perturbation theory with the GW approximation.[59,60] In the GW@PBE approximation, the electronic self-energy is approximated by a product of the single-particle Green's function (G) and the screened Coulomb potential (W). We carefully tested the grid of calculations, the energy cutoff of the response functions $E_\varepsilon$, and the number of empty states $N$ in order to converge GW calculations. Due to the error cancellation related to this kind of test, band-gap converges were employed.[61] On top of the GW quasiparticle band structure, the excitonic properties are determined by solving the Bethe–Salpeter equation (BSE)[62] using the Tamm-Dancoff approximation[63] in which local-field effects are included at the Hartree level only. The indirect transitions are not included in the present study. The frequency-dependent dielectric function was calculated using single-shot GW ($G_0W_0$),[64,65] the independent particle method (IPA),[66,67] the random phase approximation (RPA),[68] and the BSE approximation.

To explore the photocatalytic properties of the $PbTiO_3$ material, a nonpolar 7 × (2 × 2) slab in the (001) direction has been built. As in the benchmark study of Eglitis and Vanderbilt,[69] we have considered both PbO and $TiO_2$ surface terminations. In order to select the size of the slab models, we have estimated the cleavage energy at 1.30 eV per cell for different slab thickness. Surfaces with the two possible terminations arise simultaneously under cleavage and the relevant cleavage energy is distributed equally between both surfaces. The slabs consist of seven alternating $TiO_2$ and PbO layers, respectively (see Fig. 2). It is noticeable that to have adequate polarization, the GGA+*U* has been used to relax the ferroelectric surfaces. Obviously, in this work, the polarization is fixed to out-of-plane downward polarization[70] to untangle and capture the essence of the effect of the strain on the catalytic properties of the investigated structures. The bulk region has been chosen to be two lattice constants thick. We have allowed the atoms located in the two outermost surface layers to relax along the three axes. The surface atoms in the slabs were fixed in their positions, while the atoms within the bulk layers were allowed to relax during the calculations. For example, on the PbO-terminated surface, the top view reveals a repeating pattern of Pb and O atoms. The topmost layer consists of oxygen (O) atoms arranged in a square lattice. The Ti–$O_2$ layer is located below the Pb–O layer, forming a grid-like pattern. At both ends of the surface cell, the topmost Pb–O layer and Ti–$O_2$ layer were allowed to move freely in all directions, while the underlying Pb–O and Ti–$O_2$ layers were kept fixed (specifically, the three Pb–O and two Ti–$O_2$ layers in the middle of the surface cell). On the other hand, the $TiO_2$-terminated slab exhibits a top view with a repeating arrangement of Ti and O atoms. Each Ti atom is surrounded by four O atoms, creating a coordination environment characteristic of $TiO_2$. In this case, the topmost Ti–$O_2$ layer and the following Pb–O layer were allowed to move, while the underlying PbO layer and the remaining $TiO_2$ layers were fixed. To reach energy minimization, we have derived the surface energy of the unrelaxed surface ($\gamma_u$) from a single-point calculation of the pristine surface before relaxation, *via* the following equation:

$$\gamma_u = \frac{E_{slab,u} - E_{bulk}}{2A} \quad (1)$$

$E_{slab,u}$ represents the total energy of the non-relaxed slab, whereas, the $E_{bulk}$ is the total energy of the bulk, which contains the same number of formula units as the slab. The *A* parameter represents the surface area of one side of the slab. As this slab model does not produce an isolated relaxed surface and both sides of the symmetric stoichiometric slabs are considered in the calculation of the energy, their surface energies ($\gamma_r$) and ($\gamma_u$), for the relaxed and unrelaxed sides, respectively, are related by the following equation:

$$\gamma_r + \gamma_u = \frac{E_{slab,r} - E_{bulk}}{A} \quad (2)$$

where $E_{slab,r}$ is the slab total energy after relaxation. In this manner, we have taken the averaged surface energy ($E_{surf}$) to characterize the stability of our investigated slabs. We have found an average surface energy ($E_{surf}$) equal to 0.94 eV per unit-cell, in fear agreement with that found by Meyer *et al.*[71] for the tetragonal structure of $PbTiO_3$ with $E_{surf}$ = 0.97 eV per unit-cell.

HER is a multistep process that takes place on the surface of the catalyst, and there are two proposed mechanisms: Volmer–Heyrovsky and Volmer–Tafel. These mechanisms describe the hydrogen atom adsorption and hydrogen molecule desorption reactions among an initial, an intermediate adsorbed state, and a final product state (see section 4). Because the initial and final states in HER are equivalent at equilibrium reduction the Gibbs free energy of the intermediate state, $|\Delta G_H|$, is considered as a descriptor of this process. In the diffidence of Helmholtz Free energy is defined as the difference between the internal energy (*U*) and the product of the absolute temperature (*T*) and the entropy (*S*) of a system. Gibbs free energy is the difference between the enthalpy (*H*) and the product of the absolute temperature (*T*) and the entropy (*S*) of a system. The Gibbs free energy corresponding to reactants and products at standard conditions is calculated using the method proposed by Nørskov *et al.*[72] In this framework, the electronic structure of the catalyst allows for the calculation of the free energy of the reaction based on the adsorption energies of the reaction intermediates:

$$\Delta G_{H*} = \Delta H - T\Delta S + \Delta E^{ZPE} \quad (3)$$

The three terms, $\Delta H$, $T\Delta S$, and $\Delta E^{ZPE}$ denote, respectively, enthalpy, entropic contributions, and zero-point energies. The three quantities are easily derived from standard thermodynamic vibrational frequency calculations[73] (see ESI† for the detailed formulation).

The binding energy, which describes the strength of the adsorption of hydrogen atoms, was evaluated as follows: $E_{ads}$ =

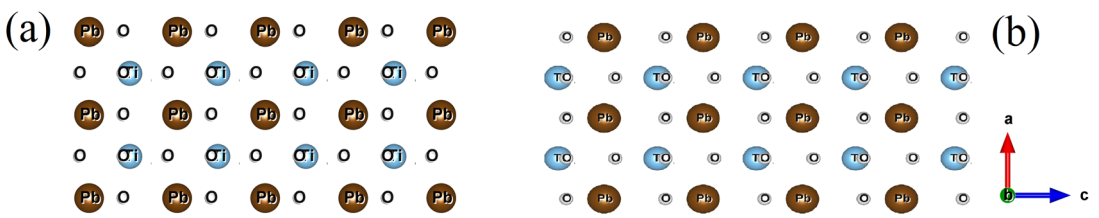


Fig. 2 Schematic illustration of the supercell geometries for the two differently terminated $PbTiO_3$ (001) surfaces, (a) PbO-terminated and (b) $TiO_2$-terminated.

$E_{slab+H} - E_{slab} - \frac{1}{2}E(H_2)$. Where $E_{slab+H}$ and $E_{slab}$ are the total energy with and without hydrogen atoms, respectively. Furthermore, lattice-dynamics calculations were performed within the density-functional perturbation theory (DFPT) implemented in VASP using the direct-force constant approach (or supercell method) to study the phonon dispersion curves including the vibrational modes at the Γ point of the Brillouin Zone.[74] The phonon dispersion spectra were evaluated and plotted using the toolkit available through the Phonopy[75] open-source code. Due to the ionic trend of the investigated compounds and in order to remove the degeneracy between the LO and TO phonons at the Brillouin zone center, the LO–TO splitting was taken into account on a 3 × 3 × 3 supercell, and this calculation was done on a grid of 4 × 4 × 3.

# 3 Results and discussion

## 3.1 The properties of tetragonal $PbTiO_3$

**3.1.1 Structural properties and stability.** We have optimized the tetragonal crystal structure of $PbTiO_3$ (space group *P*4*mm*). From total-energy calculations, we also obtained the Bulk modulus ($B_0$) and its pressure derivative $B'_0$. The optimized lattice and equation of state parameters are gathered together in Table 1 where they are compared with previous experiments[15,16,76] and calculations.[19,77] The agreement with previous studies is good. In addition, the calculated bulk modulus (59.22 GPa) agrees well with previous experiments ($B_0$ = 60 GPa),[78] giving a match the better description of the bulk modulus than previous computing simulations; $B_0$ = 35 [79] and $B_0$ = 135 GPa.[80] Due to the good agreement between our calculations and experiment, we can claim that our GGA+*U* optimization describes well the crystal structure and mechanical properties on tetragonal $PbTiO_3$. We cannot exclude some overestimation of the c lattice parameter and the conventional trend of the use of the GGA calculations. However, the result shows a better agreement with the experiment than the calculated ones by the same approximation as ref. 28.

We have also calculated the phonon dispersion of tetragonal $PbTiO_3$ to check its dynamical stability. We present in Fig. S2 of the ESI,† the result along the corresponding Brillouin zone. We also include in the figure the calculated phonon density of states (PhDOS). A global view of the full phonon dispersion spectrum probes the absence of imaginary branches, supporting the dynamical stability of tetragonal $PbTiO_3$.[81] The unit cell has five atoms, so there are 15 vibrational modes. These modes obey the following factor group analysis at the Γ point: $\Gamma_{acoustic} + \Gamma_{optic} = (A_1 + E) + (3A_1 + B_1 + 4E)$. Three modes are acoustic vibration (one $A_1$ and one E) and twelve are optic vibrations ($3A_1 + B_1 + 4E$). The modes E are doublets. The optical $A_1$ and E modes are both Raman and IR active, while the $B_1$ mode is only Raman active. Table 2 summarizes the calculated modes compared with previous studies. Our calculated modes are in good agreement with previous calculations,[82] with some small differences in phonon frequencies due to different exchange correlations used. The comparison with experiments[83] is also very good, with a difference below 15% which is comparable to typical differences between calculated and measured phonon frequencies in ternary oxides.[84] From the PhDOS it can be concluded that the lowest frequency optical mode corresponds to movements of Pb atoms, while the rest of the modes are associated with vibrations of the $TiO_6$ octahedron.

The elastic constants ($C_{ij}$) of $PbTiO_3$ have been also calculated. In its tetragonal crystal structure, the elastic constants may be reduced to six independent elastic components,[85]

**Table 2** Calculated phonon modes as well as their assignment and activity compared to the literature

| Symmetry | $\omega$ (cm$^{-1}$) Theory This work | $\omega$ (cm$^{-1}$) Experiment Ref. 83 | $\omega$ (cm$^{-1}$) Calculations Ref. 82 | Activity |
|---|---|---|---|---|
| E | 84.38 | 88 | 94.48 | R/IR |
| $A_1$ | 146.18 | 149 | 152.51 | R/IR |
| E | 190.36 | 220 | 211.0 | R/IR |
| $B_1$ | 263.56 | 289 | 270.86 | R |
| E | 266.13 | 289 | 273.08 | R/IR |
| $A_1$ | 364.09 | 359 | 367.41 | R/IR |
| E | 471.09 | 506 | 494.49 | R/IR |
| $A_1$ | 675.34 | 644 | 678.54 | R/IR |

**Table 1** Calculated lattice parameters, bulk modulus ($B_0$ in GPa) and its derivative ($B'_0$), and elastic constants. The bulk modulus *B* (in GPa), shear modulus *G* (in GPa), Young modulus *E* (in GPa), Vickers hardness HV (in GPa), *B*/*G* ratio, obtained from the elastic constants using Voigt, Reuss, and Hill approximations are also included. Results are compared with the literature

| | *a* (Å) | *c* (Å) | $B_0$ | $B'_0$ | $C_{11}$ | $C_{12}$ | $C_{13}$ | $C_{33}$ | $C_{44}$ | $C_{66}$ |
|---|---|---|---|---|---|---|---|---|---|---|
| GGA+*U* (this work) | 3.91 | 4.34 | 59.22 | 3.41 | 214.16 | 93.16 | 61.75 | 30.45 | 43.13 | 94.50 |
| Experiment (ref. 16) | 3.90 | 4.16 | | — | — | — | — | — | — | — |
| Experiment (ref. 76) | — | — | — | — | 235 | 105 | 101 | 98 | 65 | 104 |
| Experiment (ref. 15) | 3.986 | 4.026 | — | — | — | | — | — | — | — |
| Theor (ref. 77) | 3.87 | 4.07 | — | — | — | — | — | — | — | — |
| Theor (ref. 19) | — | — | — | — | 229.00 | 95.60 | 64.30 | 41.20 | 47.20 | 98.60 |
| GGA+*U* (ref. 28) | 3.85 | 4.72 | — | — | | | | | | |

| | *B* | *G* | *E* | $\nu$ | *B*/*G* | HV |
|---|---|---|---|---|---|---|
| Voigt | 99.122 | 52.293 | 133.417 | 0.276 | 1.896 | 6.529 |
| Reuss | 14.289 | 11.996 | 28.118 | 0.172 | 1.191 | 3.942 |
| Hill | 56.706 | 32.144 | 81.108 | 99.565 | 1.764 | 4.802 |

which are summarized in Table 1. The results fulfill the Born stability criteria for tetragonal structures given in eqn (4):[86–88]

$$C_{11} > C_{12}, 2C_{13}^2 < C_{33}(C_{11}+C_{12}), C_{44} > 0, C_{66} > 0 \quad (4)$$

Thus, the tetragonal structure is also mechanically stable at zero pressure. From the elastic constants, using the Voig,[89] Reuss,[90] and Hill[91] approximations, we have calculated, the bulk ($B$), shear ($G$), and young ($E$) modulus. We have also determined the Poisson ratio ($\nu$), anisotropy ratio ($B/G$), and Vickers hardness (HV). Results are given in Table 1. Our elastic constants are compatible with previous experiments and calculations as can be seen in Table 1. Notice that $C_{11}$ is larger than the other calculated $C_{ij}$ components. In particular, $C_{11}$ is 7 times larger than $C_{33}$ which is indicative of an anisotropic response to compression, being the $c$-axis the most compressible direction. In the same manner, $C_{11}$ is 2 times larger than the $C_{12}$, which makes $PbTiO_3$ in the $ab$-plane more compressible along the (100)/(010) directions than along the (110) direction. On top of that $C_{44} < C_{66}$, which indicates that the [010](001) shear is easier than the [100](010) shear. A consequence of it is the fact that the shear modulus is much smaller than the bulk and young modulus $E$ (see Table 1). On the other hand, when the bulk modulus obtained from an elastic constant is compared with experiments ($B_0$ = 60 GPa)[78] and the value obtained from our total-energy calculations ($B_0$ = 59.2 GPa), it can be seen from Table 1, that the Hill approximation (which gives $B$ = 56.7 GPa) describes more accurately the bulk modulus than the Voigt and Hill approximations. According to the Hill approximation, the ratio of ($B/G$) is 1.764, which is very close to the value proposed by Pugh (1.75)[92] to discriminate between a brittle and a ductile behavior of materials. Thus $PbTiO_3$ cannot be described either as brittle or a ductile. Finally, the values obtained for the Vickers hardness HV suggest that the investigated compound has a similar hardness to Apatite and other phosphates.[93]

**3.1.2 Electronic properties.** Due to the $3d^2$ electronic configuration of Ti atoms, the oxygen 2p subspaces in O atoms and the lack of inversion symmetry in the investigated compound, the effect of spin–orbit coupling (SOC) could be particularly relevant in the electronic properties. To analyze this effect, we have used the GGA+$U$ method with and without including the SOC effect, to calculate the band structure as well as the partial electronic density of states (PDOS). We should note that we have used the same optimized unit-cell obtained from GGA+$U$ calculations. Fig. 3 presents both the GGA+$U$ and GGA+$U$+SOC calculations of the band structure along the high-symmetry directions of the Brillouin zone (BZ). In both cases, the band structure has a phonon-assisted indirect band gap. As shown in Fig. 3, we have found that SOC has a minor effect, affecting only the conduction band minimum (CBM) along the R → Z and Γ → M directions. As a consequence, the spin–orbit coupling has little influence on the electronic properties, with a slight splitting equal to 20 meV (see Table 3 and Fig. S3 in the ESI†). This phenomenon is due to the Rashba–Dresselhaus effect.[94] Even though the splitting is present in the upper level of the condition band, the flat level (Γ → Z) dispersion of the CBM seems not to be affected by SOC. The value of the indirect band-gap energy is, respectively $E_g$(GGA+$U$+SOC) = 2.93 and $E_g$(GGA+$U$) = 2.95 eV. Both values agree well with the recently reported experimental band-gap value of 3.097 eV.[22] The band gap was also calculated

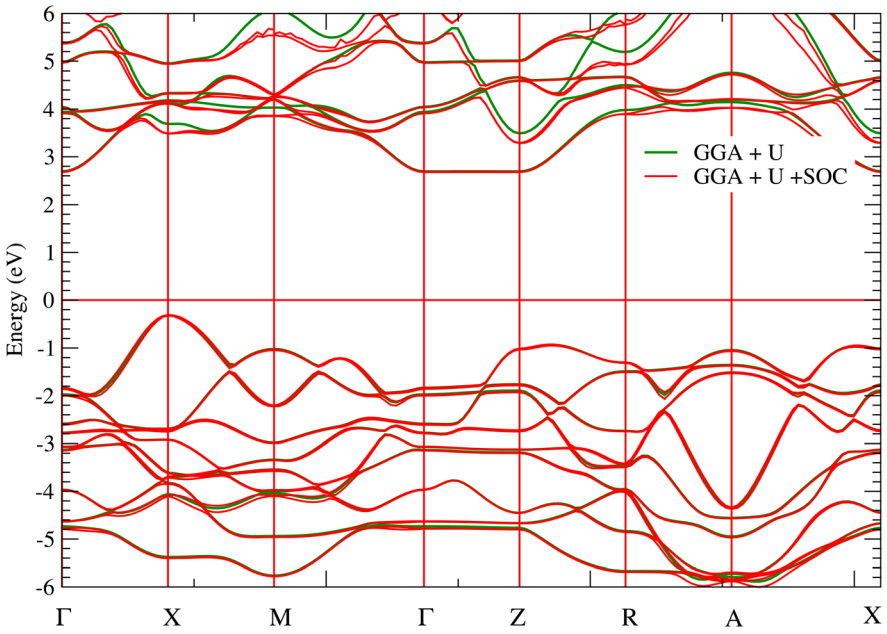


Fig. 3 Band structure calculated using the GGA+$U$. The green line shows the band structure calculated without the SOC correction and the red one the band structure calculated including the SOC correction.

Table 3 Calculated band gap of $PbTiO_3$ using GGA+*U*, GGA+*U*+SOC, and $G_0W_0$. The results are compared to previous theoretical and experimental results. The table also contains the effective masses of the holes ($m_h^*(m_0)$) and electrons ($m_e^*(m_0)$), the recombination rate ($m_h^*/m_e^*$), and the exciton binding energy ($E_b$) (meV). The values $^{WM}$ and $^{BSE}$ correspond to those calculated using the two-band Wannier–Mott and quasi-particle-BSE correction model. The macroscopic dielectric function $\varepsilon_\infty$ has been computed within the standard random-phase approximation (RPA), and the effective masses of carriers have been extracted from band structures of the Wannier function. (0%) and (±5%) correspond respectively to pristine and stained structures. The effective masses, the macroscopic dielectric function $\varepsilon_\infty$ and the exciton binding energy ($E_b$) are calculated with the $G_0W_0$ approach

| | $E_g$ (eV) | $m_h^*(m_0)$ | $m_e^*(m_0)$ | $m_h^*/m_e^*$ | $\varepsilon_\infty$ | $E_b$ (meV) |
|---|---|---|---|---|---|---|
| (0%) | 2.95 | 1.19[a], 0.87[b] | 2.07[c], 1.68[d] | 0.46 | 6.99 | $185^{WM}/172^{BSE}$ |
| (−5%) | 2.63 | 1.07[a], 1.25[b] | 2.46[c], 1.09[d], 73.64[e] | 0.045 | 6.44 | $360^{WM}/320^{BSE}$ |
| (+5%) | 2.93 | 1.85[a], 1.68[b] | 1.63[f], 1.67[g] | 1.67 | 6.66 | $261^{WM}$ |
| $V_O$ | 1.30 | 2.25[h], 10.51[i] | 0.77[j], 2.70[k] | 3.66 | 18.72 | $53^{WM}$ |
| GGA+*U*+SOC (0%) | 2.93 | — | — | — | — | — |
| $G_0W_0$ (0%) | 2.89 | — | — | — | — | — |
| Exprt[22] (0%) | 3.097 | — | — | — | — | — |

[a] Corresponds to the X → M direction. [b] Corresponds to the X → Γ direction. [c] Corresponds to the Z → A direction. [d] Corresponds to the Z → R direction. [e] Corresponds to the Z → Γ direction. [f] Corresponds to the Γ → X direction. [g] Corresponds to the Γ → M direction. [h] Corresponds to the A → Z direction. [i] Corresponds to the A → R direction. [j] Corresponds to the M → X direction. [k] Corresponds to the A → Γ direction.

within the GW approach. The obtained value is 2.89 eV (see Table 3 for a comparison of different results). This prediction is less accurate than the GGA+*U* one.

The fundamental band gap of $PbTiO_3$ has an indirect nature, being the maximum of the valence band at the X point of the BZ and the minimum of the conduction band at the Γ of the BZ. To deeply understand the contribution of each orbital in the band structure, we will continue our considerations from the examination of the PDOs calculated using GGA+*U*+SOC; see Fig. 4. Surprisingly, the $6s^2$-Pb orbitals play a dominant role. In fact, the investigated compound adopts a $Ti^{4+}Pb^{2+}O^{2-}$ configuration, so its Pb atoms have a $d^{10}s^2\ p^0$ electronic configuration. This fact creates a stereo-active lone electron pair rationalized by the stabilization caused by a localized hybridization of the occupied $s^2$ and empty $p^0$ valence orbitals. This phenomenon leads to an on-site second-order Jahn–Teller effect,[7] leading to the above-described strong distortion in the $TiO_6$ coordination octahedron. The $6s^2$-Pb orbitals play a key role in the electronic properties of the compound. The PDOS plot also reveals that the electronic configuration of $PbTiO_3$ is governed by an O-p state near the Fermi level ($E_F$), hybridized with the Ti-d one. In contrast, the plot hosts weak contributions of d states of the lead atom near the $E_F$ level.

### 3.2 The effect of bi-axial compressive strains

We will now discuss the effect of biaxial strains on the electronic properties. Due to the possible development of zone-boundary instabilities[95] in $PbTiO_3$, and the phase transitions that take place at 10 GPa,[96,97] in calculations, the strain applied in calculations is constrained to not exceed that value. We present in Fig. 5(a) the evolution of both lattice parameters and band-gap energy as a function of the bi-axial strain. To make a comparison, we have also taken care to include the effect of the hydrostatic strains. We have found that in both hydrostatic and non-hydrostatic conditions, the band gap undergoes a sharp reduction of ∼0.5 eV (see Fig. 5(b), (c) and also Fig. S5 in the ESI†). This result is related to the tetragonal symmetry, the piezoelectric trend,[97] as well as the strong anisotropic behavior of $PbTiO_3$. The hydrostatic compression in the lattice constant '*a*' from 0 to 10 GPa is about −5%, which is in fair agreement with the result found when applying the $\sigma_{xy}$ strain.

### 3.3 The excitonic binding energy

To gain deeper insight into the role of exciton binding energy on the HER activity of $PbTiO_3$, we have used two methods, an estimation by means of calculations based on the Bethe–Salpeter equation (BSE) and an estimation within the two-band model of Wannier–Mott.[98,99] (Due to the enormous cost of calculation, the estimation of exciton binding energy within the Bethe–Salpeter equation has been made only for unstrained structures and compared with those estimated by the second method for strained ones.). We have employed the many-electron GW method to calculate the quasi-particle energies and band gaps ($E_g$). To obtain an accurate electronic structure, convergence tests have been carried out on the grid of calculations (*k* grid), the number of empty states (*N*), and the energy cutoff of the response functions ($E_\epsilon$).[100] The effective masses for the electrons ($m_e^*$) and holes ($m_h^*$), relative to the free electron mass ($m_0$), have been estimated along the highly symmetric *k*-path at band edges and depicted in Table 3. According to Fig. S7 of the ESI,† there are 800 empty bands, a dielectric cutoff energy of 600, and a grid of 4 × 4 × 3 are sufficient for converging the BSE calculations.

The results of the calculated exciton-binding energies ($E_b$) with both the BSE and Wannier–Mott models are summarized in Table 3. We have found large exciton binding energies for both zero pressure and strained structures. The large value of exciton binding energy requires important energy to dissociate the electron–hole pair, which in turn leads to high photocatalytic properties. We should note that the polaronic effects are beyond the scope of our study. The exciton binding energies calculated by BSE are estimated by evaluating the energy difference between the IPA-$G_0W_0$ band gap and the first bright

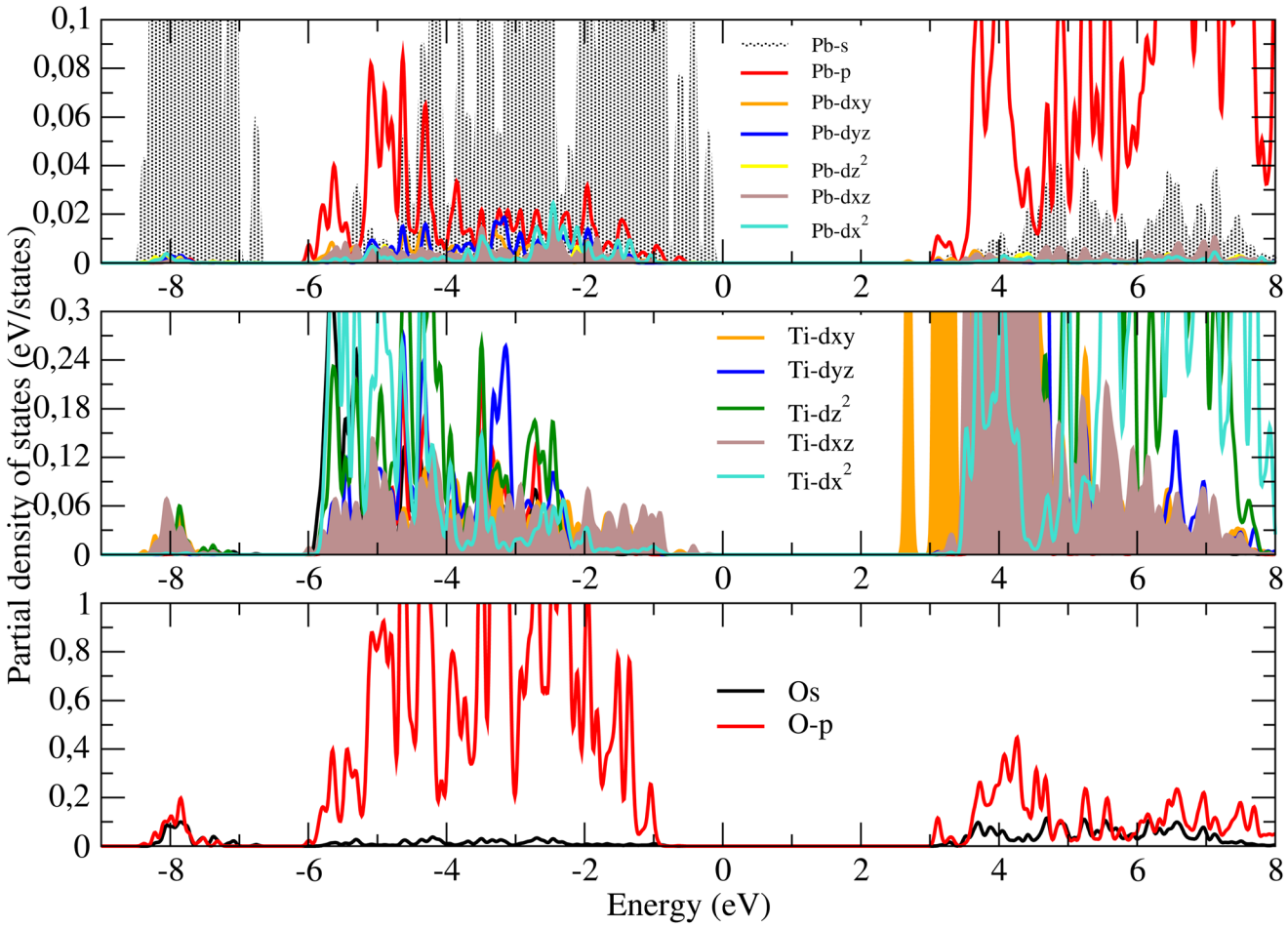


**Fig. 4** Partial electronic densities of states (PDOS) of $PbTiO_3$ calculated using GGA+*U* and including the SOC.

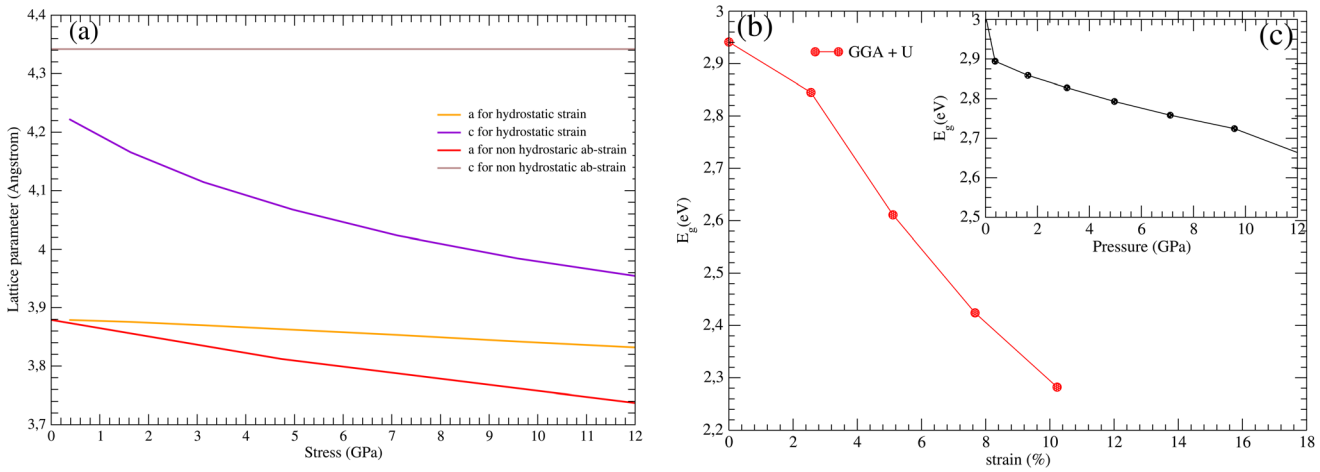


**Fig. 5** (a): The evolution of GGA+*U* *a* and *b* lattice parameters under compressive strain for both biaxial and hydrostatic cases. (b): The evolution GGA+*U* band-gap energy ($E_g$) under biaxial strain and (c) under hydrostatic strain.

$G_0W_0$@BSE eigenvalue (see the adsorption spectrum of Fig. S8 in the ESI†). Notably, the $E_b$ estimated within the Wannier–Mott model by the effective mass approximation is very close to the one calculated by the BSE correction, which suggests that the use of this method to calculate $E_b$ for strained structures does not diminish its consistency. Therefore, one can

conclude that the application of strain increases the value of $E_b$. This trend can be understood in terms of the increase in local distortions in $TiO_5$ units. To check this hypothesis, we have also applied a tensile strain to $PbTiO_3$. The result has shown qualitatively similar behavior to that under compression on the electronic properties of the investigated material, but the band gap decreased more weakly for tensile deformations than in the case of compression; see Table 3.

### 3.4 Catalytic properties of $PbTiO_3$

To evaluate the catalytic properties of $PbTiO_3$ slabs, we have analyzed different possible adsorption sites of the H atom on both PbO-terminated and $TiO_2$-terminated surfaces including the oxygen top site, titanium top site, oxygen–titanium bridge site, and hollow site above the subsurface lead. Some possible surface adsorption configurations considered are shown in Fig. 6 and their adsorption energies are also displayed in Table S1 of the ESI.† Evidently, the H atoms react favorably on the top of the oxygen atom; however, the more dominant interaction is shown on the top of the Pb atom on the PbO-terminated surface and the Ti atom on the $TiO_2$-terminated surface. However, during the relaxation process, we noticed that the PbO-terminated surface is not stable with regard to hydrogen adsorption. The DFT relaxation of the slab ended up with an important local distortion, which drives the reduced surface layer to undergo reconstruction. In most cases, we have a rapid formation of the O–H bonds (see Fig. 7). This fact should facilitate the formation of the water molecule during the Tafel step. Tests were thus realized to check this trend by evaluating the strength of the adsorption of the OH molecule on the PbO-terminated surface. The energy adsorption has been found to equal ≃−3 eV, an indication of the strong reactivity of the OH molecule with this surface. O–H bond formation can lead to the formation of adsorbed hydroxyl groups on the catalyst surface. These hydroxyl groups can block the active sites of the catalyst, reducing its efficiency and leading to catalyst deactivation. This effect is particularly significant when the catalyst material is susceptible to surface oxidation or when the

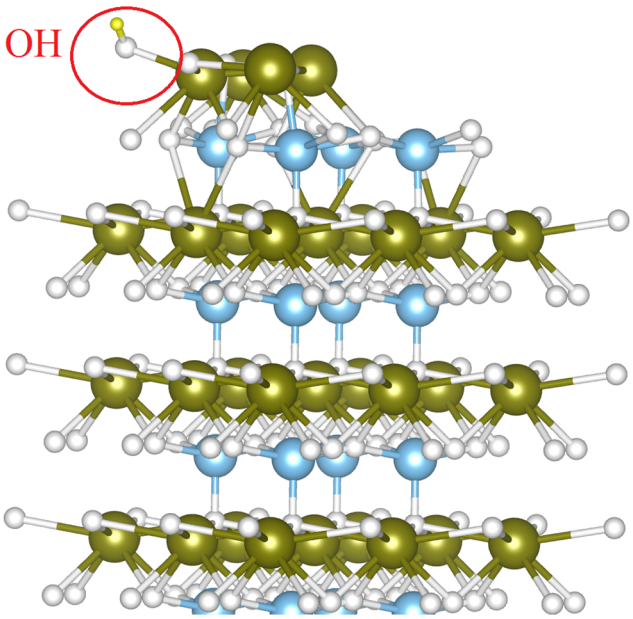


Fig. 7 The formation of OH molecule on the Pb-terminated surface of the $PbTiO_3$ slab.

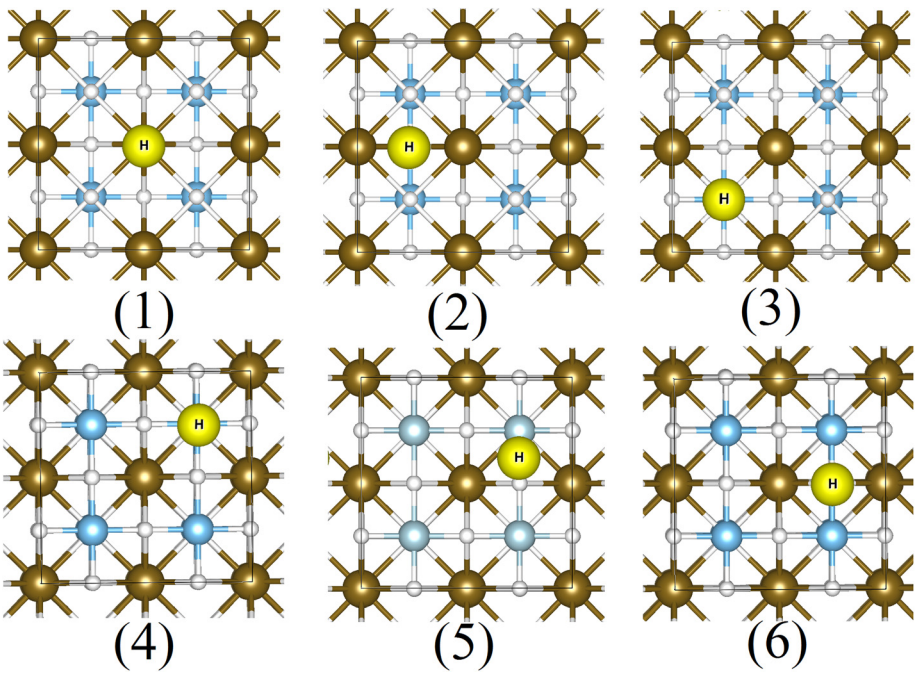


Fig. 6 The optimized adsorption states on the $TiO_2$-terminated surface of the $PbTiO_3$ slab.

concentration of hydroxyl groups becomes high. This trend explains why the most popular study method is the use of vacancies to study the reactivity of hydrogen atoms on the PbO-terminated surface of the $PbTiO_3$ slab (see work of ref. 44 and 17). This electrochemical instability is also mentioned in.[101] In fact, the strong acid environment of this thermodynamic state is not desirable for pH-universal HER catalysis,[70] which favors rather the study of $TiO_2$—terminated surfaces for such a mechanism. Therefore, due to the fact that catalytic stability is an important figure of merit for a stable catalyst, only the $TiO_2$-terminated surface will be considered for the rest of the study.

As it is known, according to Nørskov *et al.*,[72] in an acidic environment, the electrocatalytic HER can carry out the reaction according to the Volmer–Heyrovsky/Tafel route, so, the reaction at equilibrium state at standard conditions (1 atm, 298.15 K), will be done according to the initial state, $G(* + H^+ + e^-)$, the intermediate state, $G(H^*)$, and the final state, $G(* + \frac{1}{2}H_2)$. Where, * represents the active site of the catalyst.[72,102,103] The reaction equations involved in HER are then given as follows:

$$* + H^+ + e^- \leftrightarrow H*, (\text{Volmer step}) \quad (5)$$

$$H* + H^+ + e^- \leftrightarrow * + H_2, (\text{Heyrovsky step}) \quad (6)$$

$$* + H_2 \leftrightarrow 2H*, (\text{Tafel step}) \quad (7)$$

To characterize the HER, the Gibbs free energy of hydrogen adsorption ($\Delta G_H$) was determined under standard conditions.[102] Because the initial and final states are equivalent at equilibrium reduction potential, $U = 0$, the Gibbs free energy of the intermediate state, $|\Delta G_H|$, has been considered as a major descriptor of the HER activity for a wide variety of catalysts. Therefore, the optimum value of $|\Delta G_H|$ should be zero for a spontaneous reaction without an activation energy barrier. Fig. 8 shows the calculated free-energy diagram. The challenge behind plotting this figure is to search for an HER with an ideal value of $\Delta G_H$ close to zero; however, we must keep in mind that an optimal catalyst for HER should be able to bind hydrogen neither too strongly nor too weakly.[102,103] $\Delta G_H > 0$ yields relatively slow kinetics in the process of hydrogen adsorption, while $\Delta G_H < 0$ gives relatively slow kinetics in the process of $H_2$ release. For this reason, we display the results of the more dominant configurations calculated for the pristine $TiO_2$—terminated surface together with the compressed and tensile ones built from the +5% and −5% strained tetragonal $PbTiO_3$ structures and the structure with defect $V_O$ site (The vacancy defect is located on the upper layer of the surface of the interacted face.). We can show clearly that while the HER activity is very close to zero for the $V_O$ structure (see Table S2 in the ESI†), the compressive strain, as well as the tensile one, drives $\Delta G_H$ to move toward a more negative value, which could reduce the HER activity. The HER over-potential seems better than that found for the $BaTiO_3$ slab modulated by polarization states.[70,104] This finding can be supported by the experimental finding of ref. 17, where the experimental evidence shows that the oxygen vacancies in $PbTiO_3$ show the spontaneous formation of active sites during preparation pro-

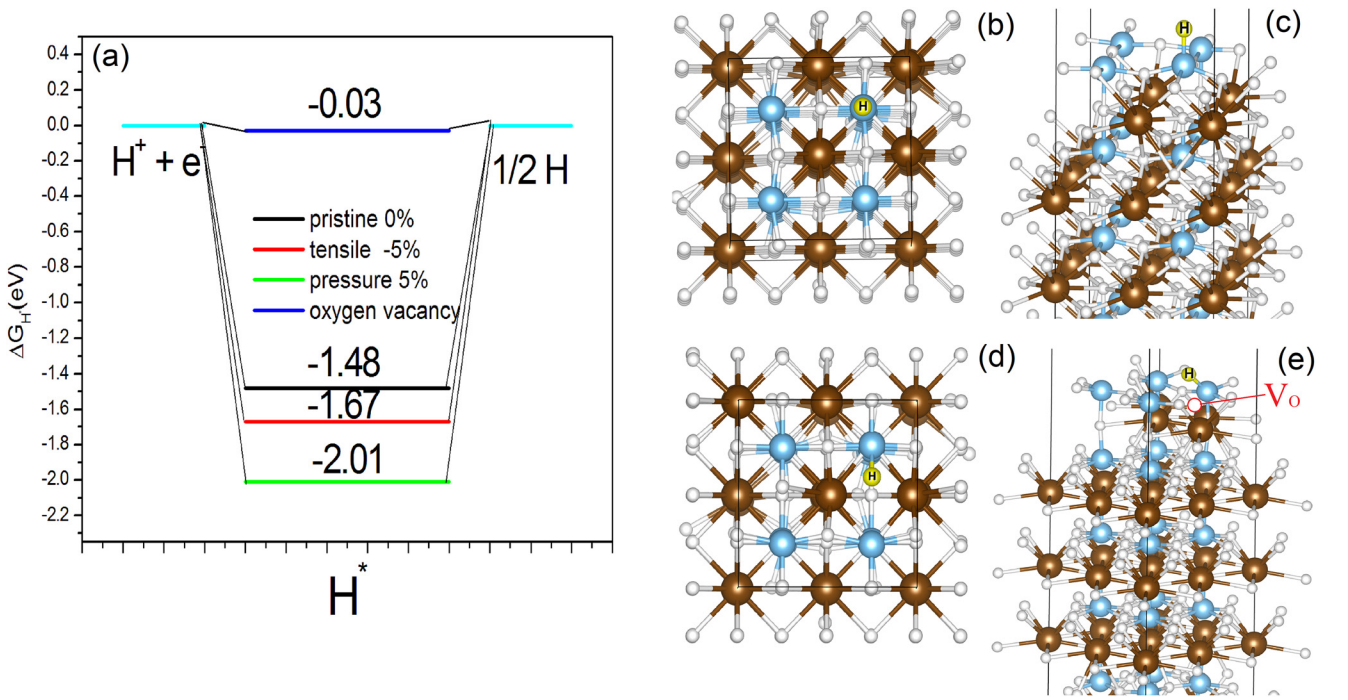


**Fig. 8** (a) The Gibbs free-energy diagram of the HER on pristine, compressive, tensile, and defective $TiO_2$-terminated surfaces at pH = 0. Elementary reaction structures of HER on the $TiO_2$-terminated surfaces. The adsorbed states are illustrated on top and perspective view for both (b) and (c) strained and (d) and (e) defective $V_O$ structures.

cedures due to their lower formation energy. Furthermore, the oxygen vacancies are mainly concentrated near the negatively polarized facet (001) of $PbTiO_3$ due to their positive charges. The treatment of the sample used with the shielding effect of external ions on the polarization field induces the formation of $TiO_2$ islands that could be selectively formed on the surface of the positively polarized facet, which is the main reason for the decrease in the overall photocatalytic activity of this compound.

To elucidate the electronic charge made behind the adsorption of a hydrogen atom on the $TiO_2$-terminated surface of the $PbTiO_3$ material, we have plotted the partial density of state (PDOS) at GGA+*U* level (see Fig. S10 and S11 of the ESI†). This allows us to get an insight into the adsorption action caused by strains and the defective site caused by $V_O$ vacancy. While the strain actions do not promote strong changes in electronic configuration, the $V_O$ one causes a remarkable change both structurally and electronically, which affects the process of adsorption of $H^+$ species. The main difference between strained and $V_O$ PDOS is elucidated by the contribution of d-Ti redistribution. In the $V_O$ case, the PDOS becomes metallic with strong d-Ti/O hybridization near the Fermi energy. In our situation, the neutral $V_O$ reduces the neighboring cations Ti with aliovalent substitution and fills partial holes in the O sp-band. It is also shown that in the adsorption of $H^+$ species in the pristine and strained slabs, the $H^+$ atom is bonded in a vertical position on top of the Ti atom. However, it is rather inclined in the case of the $V_O$ one. If we refer to what was elucidated in the former sections, we see that both pristine and strained structures have strong, exciting energy thus less chance of being used for photocatalytic mechanisms. The calculated adsorption energies also show strong adsorption of $H^+$ species on their surfaces. Consequently, the HER reaction is not suitable for these cases. However, in the case of the $V_O$ structure, the incorporation of oxygen vacancies into our oxide showed a decrease in the coordination number of active metal sites, namely the Ti one, suggesting a delocalization of the electrons neighboring oxygen vacancies, which facilitates the electron transport from $H^+$ to the surface. Albeit, we have moderate adsorption energy and a moderate $E_B$ value, indicating that the zero band gap active site is more favorable to the HER process as well as photocatalytic applications.

# 4 Conclusions

In order to examine the catalytic properties as well as their trend as regards bi-axial strain and the incorporation of oxygen vacancy in tetragonal $PbTiO_3$, density-functional theory calculations have been carried out. Our results show the dynamical and mechanical stability of the investigated compound in its tetragonal structure (space group *P4mm*). The structure of $PbTiO_3$ shows a lone pair in the Pb orbital; this induces a polyhedral distortion by the on-site second-order Jahn–Teller effect. The wide band gap is then easily tuned by bi-axial compression. The applied bi-axial compression increases the distortion of the $TiO_6$ units and also the excitonic binding energy. We have also checked the effect of an oxygen vacancy on the bulk structure of $PaTiO_3$. The formation energy has shown favorable energy and a rearrangement of the electronic orbitals. The electronic configuration changed from $3d^0$ to $3d^2$ and is localized at the Fermi level. This results in a strong decrease of the band gap. The defective $V_O$ structure has shown a rather moderate exciting binding energy value compared to the pristine and strained structures.

In the second part of the work, we have simulated two stabs, the former with a PbO-terminated surface and the second with the $TiO_2$-terminated one. The calculation of adsorption energy has shown a strong distortion on the PbO-terminated surface, which shows instability when the H atom is adsorbed. These results lead us to dismiss this surface from the analysis of the HER process. However, both pristine and strained $TiO_2$-terminated samples manifested strong adsorption on the $H^+$ species, which makes them not favorable for the HER process. While the $V_O$ surface shows a favorable HER, we stipulate that due to the favorable condition, namely moderate exciting binding energy necessary for photocatalytic applications as well as the binding one as regards the reactivity to $H^+$ species. In fact, higher exciting energy is typically associated with a higher rate of electron transfer, which can improve the efficiency of HER. Alternatively, if the exciting energy required for electron transfer is too high, the reaction may be slower or inhibited. So, the $V_O$ surface of $PbTiO_3$ with moderately exciting binding energy is the more promising platform for catalytic and photocatalytic reactions.

# Author information

Readers are welcome to comment on the online version of the paper. Correspondence and requests for materials should be addressed to T. O. (tarik_ouahrani@yahoo.fr) and Daniel Errandonea (daniel.errandonea@uv.es).

# Data availability

The data that support the findings of this study are available from the corresponding author upon reasonable request.

# Conflicts of interest

The author declares that he has no known competing financial interests or personal relationships that could have appeared to influence the work reported in this paper.

# Acknowledgements

T. O. acknowledges the financial support given by the Laboratory of Theoretical Physics of the University of Tlemcen, and thanks for the financial support obtained through PRFU

B00L02EP130220230001. A. M.-G. thanks the support to the Spanish MICIN and AEI (https://doi.org/10.13039/501100011033) through the projects PID2020-115293RJ-I00, PID2021-126076NB-I00, TED2021-129506B-C22, and María de Maeztu CEX2021-001202-M. This work was granted access to the HPC resources of TGCC under the allocation 2021-A01008104333 made by GENCI. D. E. thanks the financial support from the Spanish Research Agency (AEI) and Spanish Ministry of Science and Investigation (MCIN) under projects PID2019106383GB-C41 and PID2022-138076NB-C41 (https://doi.org/10.13039/501100011033) and MALTA Consolider Team network, under projects RED2018-102612-T and RED2022-134388-T. This work was also partially supported by the Generalitat Valenciana under Grant No. PROMETEO CIPROM/2021/075-GREENMAT. This study forms part of the Advanced Materials Programme and was supported by MCIN with funding from European Union NextGenerationEU (PRTR-C17.I1) and by Generalitat Valenciana (Grant MFA/2022/007). R. F. acknowledges financial support from the Spanish National Research Agency (AEI) through projects PID2021-122588-NB-C21.

## References

1 A. Ennaoui, S. Fiechter, C. Pettenkofer, N. Alonso-Vante, K. Büker, M. Bronold, C. Höpfner and H. Tributsch, Iron disulfide for solar energy conversion, *Sol. Energy Mater. Sol. Cells*, 1993, **29**, 289–370, DOI: 10.1016/0927-0248(93)90095-K.

2 R. Murphy and D. R. Strongin, Surface reactivity of pyrite and related sulfides, *Surf. Sci. Rep.*, 2009, **64**, 1–45, DOI: 10.1016/j.surfrep.2008.09.002.

3 A. Zunger, S. Wagner and P. M. Petroff, New materials and structures for photovoltaics, *J. Electron. Mater.*, 1993, **22**, 3–16, DOI: 10.1007/BF02665719.

4 M. G. Walter, E. L. Warren, J. R. McKone, S. W. Boettcher, Q. Mi, E. A. Santori and N. S. Lewis, Solar water splitting cells, *Chem. Rev.*, 2010, **110**, 6446–6473, DOI: 10.1021/cr1002326.

5 J. Quílez-Bermejo, S. García-Dalí, A. Daouli, A. Zitolo, R. L. S. Canevesi, M. Emo, M. T. Izquierdo, M. Badawi, A. Celzard and V. Fierro, Advanced Design of Metal Nanoclusters and Single Atoms Embedded in $C_1N_1$-Derived Carbon Materials for ORR, HER, and OER, *Adv. Funct. Mater.*, 2023, **33**, 2300405, DOI: 10.1002/adfm.202300405.

6 Y. Zhou, Z. Zhou, M. Chen, Y. Zong, J. Huang, S. Pang and N. P. Padture, Doping and alloying for improved perovskite solar cells, *J. Mater. Chem. A*, 2016, **4**, 17623–17635, DOI: 10.1039/C6TA08699C.

7 S. Bouguima, T. Ouahrani, A. Bouheddadj, M. Le Roux, D. Errandonea and M. Badawi, Understanding the optical and bonding properties of hybrid metal-halide ($C_5H_{16}NP$)$PbX_4$ (X = Cl, Br, I) perovskite: A density-functional theory study, *Inorg. Chem. Commun.*, 2021, **130**, 108721, DOI: 10.1016/j.inoche.2021.108721.

8 S. Belarouci, T. Ouahrani, N. Benabdallah, A. Morales-García and I. Belabbas, Two-dimensional silicon carbide structure under uniaxial strains, electronic and bonding analysis, *Comput. Mater. Sci.*, 2018, **151**, 288–295, DOI: 10.1016/j.commatsci.2018.05.020.

9 S. Patel, U. Dey, N. P. Adhikari and A. Taraphder, Electric field and strain-induced band-gap engineering and manipulation of the Rashba spin splitting in Janus van der Waals heterostructures, *Phys. Rev. B*, 2022, **106**, 035125, DOI: 10.1103/PhysRevB.106.035125.

10 A. M. Glass, D. von der Linde and T. J. Negran, High-voltage bulk photovoltaic effect and the photorefractive process in $LiNbO_3$, *Appl. Phys. Lett.*, 1974, **25**, 233–235, DOI: 10.1063/1.1655453.

11 Y. Cui, J. Briscoe and S. Dunn, Effect of Ferroelectricity on Solar-Ligh-Driven Photocatalytic Activity of $BaTiO_3$ Influence on the Carrier Separation and Stern Layer Formation, *Chem. Mater.*, 2013, **25**, 4215–4223, DOI: 10.1021/cm402092f.

12 G. Liu, L. Ma, L.-C. Yin, G. Wan, H. Zhu, C. Zhen, Y. Yang, Y. Liang, J. Tan and H.-M. Cheng, Selective Chemical Epitaxial Growth of $TiO_2$ Islands on Ferroelectric $PbTiO_3$ Crystals to Boost Photocatalytic Activity, *Joule*, 2018, **2**, 1095–1107, DOI: 10.1016/j.joule.2018.03.006.

13 H. Matsuo, Y. Noguchi and M. Miyayama, Gap-state engineering of visible-light-active ferroelectrics for photovoltaic applications, *Nat. Commun.*, 2017, **8**, 207, DOI: 10.1038/s41467-017-00245-9.

14 A. M. Glazer and S. A. Mabud, Powder profile refinement of lead zirconate titanate at several temperatures. II. Pure $PbTiO_3$, *Acta Crystallogr., Sect. B: Struct. Crystallogr. Cryst. Chem.*, 1978, **34**, 1065–1070, DOI: 10.1107/S0567740878004938.

15 G. Shirane, R. Pepinsky and B. C. Frazer, X-ray and neutron diffraction study of ferroelectric $PbTiO_3$, *Acta Crystallogr.*, 1956, **9**, 131–140, DOI: 10.1107/S0365110X56000309.

16 S. A. Mabud and A. M. Glazer, Lattice Parameters and Birefringence in $PbTiO_3$ Single Crystals, *J. Appl. Crystallogr.*, 1979, **12**, 49–53, DOI: 10.1107/S0021889879011754.

17 G. Wan, L. Yin, X. Chen, X. Xu, J. Huang, C. Zhen, H. Zhu, B. Huang, W. Hu, Z. Ren, H. Tian, L. Wang, G. Liu and H.-M. Cheng, Photocatalytic Overall Water Splitting over $PbTiO_3$ Modulated by Oxygen Vacancy and Ferroelectric Polarization, *J. Am. Chem. Soc.*, 2022, **144**, 20342–20350, DOI: 10.1021/jacs.2c08177.

18 J. W. Bennett, I. Grinberg and A. M. Rappe, New highly polar semiconductor ferroelectrics through d8 Cation-O vacancy substitution into $PbTiO_3$: a theoretical study, *J. Am. Chem. Soc.*, 2008, **130**(51), 17409–17412, DOI: 10.1021/ja8052249.

19 C. Lu, J. Wang, P. Wang, X. Xia, Y. Jin, P. Li and G. Bao, New insight into the structural evolution of $PbTiO_3$: an

 

unbiased structure search, *Phys. Chem. Chem. Phys.*, 2017, **19**, 1420–1424, DOI: 10.1039/C6CP07624F.

20 E. Horváth, M. Kollár, P. Andričević, L. Rossi, X. Mettan and L. Forró, Fighting Health Hazards in Lead Halide Perovskite Optoelectronic Devices with Transparent Phosphate Salts, *ACS Appl. Mater. Interfaces*, 2021, **13**(29), 33995–34002, DOI: 10.1021/acsami.0c21137.

21 Y. Xue, Y. Guo and C. Geng, Functionalization of two-dimensional $PbTiO_3$ film by surface modification: A first-principles study, *Appl. Surf. Sci.*, 2021, **563**, 150268, DOI: 10.1016/j.apsusc.2021.150268.

22 H. Lemziouka, L. H. Omari, R. Moubah, A. Boutahar, S. Bahhar, M. Abid and H. Lassri, Structural, dielectric and optical properties of Cu-doped $PbTiO_3$ ceramics prepared by sol–gel, *Mater. Today: Proc.*, 2021, **37**, 3940–3945, DOI: 10.1016/j.matpr.2020.09.094.

23 E. C. Paris, M. F. C. Gurgel, T. M. Boschi, M. R. Joya, P. S. Pizani, A. G. Souza, E. R. Leite, J. A. Varela and E. Longo, Investigation on the structural properties in Er-doped $PbTiO_3$ compounds: A correlation between experimental and theoretical results, *J. Alloys Compd.*, 2008, **462**, 157–163, DOI: 10.1038/nmat4765.

24 X. Chen, A. Zhang, J. Wang, Q. Luo, G. Tang, J. Zhang and D. Bai, Band alignments and polarization properties in ZnO $(11\bar{2}0)$/$PbTiO_3$ (001) heterostructures, *Vacuum*, 2019, **166**, 264–269, DOI: 10.1016/j.vacuum.2019.05.013.

25 M. F. C. Gurgel, E. C. Paris, J. W. M. Espinosa, C. O. Paiva-Santos, E. R. Leite, A. G. Souza, J. A. Varela and E. Longo, Jahn–Teller effect on the structure of the Sm-doped $PbTiO_3$: A theoretical approach, *J. Mol. Struct.: THEOCHEM*, 2007, **813**, 33–37, DOI: 10.1016/j.theochem.2007.02.017.

26 L. Wang, P. Yuan, F. Wang, E. Liang, Q. Sun, Z. Guo and Y. Ji, First-principles study of tetragonal $PbTiO_3$: Phonon and thermal expansion, *Mater. Res. Bull.*, 2014, **49**, 509–513, DOI: 10.1016/j.materresbull.2013.08.075.

27 M.-J. Zhou, Y. Wang, Y. Ji, Z.-K. Liu, L.-Q. Chen and C.-W. Nan, First-principles lattice dynamics and thermodynamic properties of pre-perovskite $PbTiO_3$, *Acta Mater.*, 2019, **171**, 146–153, DOI: 10.1016/j.actamat.2019.04.008.

28 N. Jaykhedkar, N. Tripathy, V. Shah, B. Pujari and S. Premkumar, A comprehensive study of pressure-dependent phase transitions in ferroelectric $PbTiO_3$, $PbZrO_3$ and $BaTiO_3$, *Mater. Chem. Phys.*, 2020, **254**, 123545, DOI: 10.1016/j.matchemphys.2020.123545.

29 S. Lazaro, E. Longo, J. R. Sambrano and A. Beltran, Structural and electronic properties of $PbTiO_3$ slabs: a DFT periodic study, *Surf. Sci.*, 2004, **552**, 149–159, DOI: 10.1016/j.susc.2004.01.041.

30 Q. Pang, J.-M. Zhang and K.-W. Xu, Structural and electronic properties of Pt monolayer adsorption on $PbTiO_3$(100) surface, *Thin Solid Films*, 2009, **517**, 6817–6823, DOI: 10.1016/j.tsf.2009.05.059.

31 D. M. Niedzwiedzki, H. Zhou and P. Biswas, Exciton Binding Energy of $MAPbI_3$ Thin Film Elucidated via Analysis and Modeling of Perovskite Absorption and Photoluminescence Properties Using Various Methodologies, *J. Phys. Chem. C*, 2022, **126**, 1046–1054, DOI: 10.1021/acs.jpcc.1c09598.

32 D. Zhang, P. Wang, J. Wang, Y. Li, Y. Xia and S. Zhan, Tailoring of electronic and surface structures boosts exciton-triggering photocatalysis for single oxygen generation, *Proc. Natl. Acad. Sci. U. S. A.*, 2021, **118**(48), e2114729118, DOI: 10.1073/pnas.2114729118.

33 T. Ouahrani, F.-Z. Medjdoub, S. Gueddida, A. L. Fernandez, R. Franco, N.-E. Benkhettou, M. Badawi, A. Liang, J. Gonzalez and D. Errandonea, Understanding the Pressure Effect on the Elastic, Electronic, Vibrational, and Bonding Properties of the $CeScO_3$ Perovskite, *J. Phys. Chem. C*, 2021, **125**, 107–119, DOI: 10.1021/acs.jpcc.0c08641.

34 Z. Zafar, S. Yi, J. Li, C. Li, Y. Zhu, A. Zada, W. Yao, Z. Liu and X. Yue, Recent development in defects engineered photocatalysts: An overview of the experimental and theoretical strategies, *Energy Environ. Mater.*, 2022, **5**, 68–114, DOI: 10.1002/eem2.12171.

35 S. Bai, N. Zhang, C. Gao and Y. Xiong, Defect engineering in photocatalytic materials, *Nano Energy*, 2018, **53**, 296–336, DOI: 10.1016/j.nanoen.2018.08.058.

36 J. Liu, Z. Wei and W. Shangguan, Defects engineering in photocatalytic water splitting materials, *ChemCatChem*, 2019, **11**, 6177–6189, DOI: 10.1002/cctc.201901579.

37 D. Strmcnik, P. P. Lopes, B. Genorio, V. R. Stamenkovic and N. M. Markovic, Design principles for hydrogen evolution reaction catalyst materials, *Nano Energy*, 2016, **29**, 29–36, DOI: 10.1016/j.nanoen.2016.04.017.

38 L. Xu, J. Zeng, Q. Li, L. Xia, X. Luo, Z. Ma, B. Peng, S. Xiong, Z. Li and L.-L. Wang, Defect-engineered 2D/2D hBN/g-$C_3N_4$, Z-scheme heterojunctions with full visible-light absorption: Efficient metal-free photocatalysts for hydrogen evolution, *Appl. Surf. Sci.*, 2021, **547**, 149207, DOI: 10.1016/j.apsusc.2021.149207.

39 A. Kumar and V. Krishnan, Vacancy engineering in semiconductor photocatalysts: Implications in hydrogen evolution and nitrogen fixation applications, *Adv. Funct. Mater.*, 2021, **31**, 2009807, DOI: 10.1002/adfm.202009807.

40 G. Wang, R. Pandey and S. P. Karna, Effects of extrinsic point defects in phosphorene: B, C, N, O, and F adatoms, *Appl. Phys. Lett.*, 2015, **106**, 173104, DOI: 10.1063/1.4919389.

41 X. Zhao, X. Yang, D. Singh, P. K. Panda, W. Luo, Y. Li and R. Ahuja, Strain-Engineered Metal-Free h-B2O Monolayer as a Mechanocatalyst for Photocatalysis and Improved Hydrogen Evolution Reaction, *J. Phys. Chem. C*, 2020, **124**, 7884–7892, DOI: 10.1021/acs.jpcc.0c00834.

42 Q. Peng, X. Weng, W. Xie, M. Ying, X. Lin, Y. Dai, Q. Yu, H. Pan, J. Liu and M. Du, Photocatalytic reduction for graphene oxide by $PbTiO_3$ with high polarizability and its electrocatalytic application in pyrrole detection, *J. Colloid Interface Sci.*, 2020, **560**, 502–509, DOI: 10.1016/j.jcis.2019.10.022.

43 J.-M. Zhang, Q. Pang, K.-W. Xu and V. Ji, First-principles study of the (110) polar surface of cubic $PbTiO_3$, *Comput.*

*Mater. Sci.*, 2009, **44**, 1360–1365, DOI: 10.1016/j.commatsci.2008.09.002.

44 E. Mete, Ş. Ellialtıoğlu, O. Gulseren and D. Uner, Elucidating the barriers on direct water splitting: Key role of oxygen vacancy density and coordination over $PbTiO_3$ and $TiO_2$, *J. Phys. Chem. C*, 2021, **125**, 1874–1880, DOI: 10.1021/acs.jpcc.0c09685.

45 P. E. Blochl, Projector augmented-wave method, *Phys. Rev. B: Condens. Matter Mater. Phys.*, 1994, **50**, 17953–17979, DOI: 10.1103/PhysRevB.50.17953.

46 G. Kresse and J. Hafner, Ab initio molecular dynamics for liquid metals, *Phys. Rev. B: Condens. Matter Mater. Phys.*, 1993, **47**, 558–561, DOI: 10.1103/physrevb.47.558.

47 S. Grimme, J. Antony, S. Ehrlich and H. Krieg, A consistent and accurate ab initio parametrization of density functional dispersion correction (*DFT–D*) for the 94 elements *H–Pu*, *J. Chem. Phys.*, 2016, **132**, 154104, DOI: 10.1063/1.3382344.

48 S. Grimme, S. Ehrlich and V. Goerigk, Effect of the damping function in dispersion corrected density functional theory, *J. Comput. Chem.*, 2019, **32**, 1456–1465, DOI: 10.1002/jcc.21759.

49 P. E. Bloch, Projector augmented-wave method, *Phys. Rev. B: Condens. Matter Mater. Phys.*, 1994, **50**, 17953–17979, DOI: 10.1103/PhysRevB.50.17953.

50 J. P. Perdew, A. Ruzsinszky, G. I. Csonka, O. A. Vydrov, G. E. Scuseria, L. A. Constantin, X. Zhou and K. Burke, Restoring the density-gradient expansion for exchange in solids and surfaces, *Phys. Rev. Lett.*, 2008, **100**, 136406, DOI: 10.1103/PhysRevLett.100.136406.

51 H. J. Monkhorst and J. D. Pack, Special points for Brillouin-zone integrations, *Phys. Rev. B: Solid State*, 1976, **13**, 5188–5192, DOI: 10.1103/PhysRevB.13.5188.

52 D. Gupta, S. R. Meher, N. Illyaskutty and Z. C. Alex, Facile synthesis of Cu2O and CuO nanoparticles and study of their structural, optical and electronic properties, *J. Alloys Compd.*, 2018, **743**, 737, DOI: 10.1016/j.jallcom.2018.01.181.

53 S. L. Dudarev, G. A. Botton, S. Y. Savrasov, C. J. Humphreys and A. P. Sutton, Electron-Energy-Loss Spectra and the Structural Stability of Nickel Oxide: An LSDA + U Study, *Phys. Rev. B: Condens. Matter Mater. Phys.*, 1998, **57**, 1505–1509, DOI: 10.1103/PhysRevB.57.1505.

54 P. Giannozzi, S. De Gironcoli, P. Pavone and S. Baroni, Ab initio calculation of phonon dispersions in semiconductors, *Phys. Rev. B: Condens. Matter Mater. Phys.*, 1991, **43**, 7231, DOI: 10.1103/PhysRevB.43.7231.

55 A. Togo and I. Tanaka, First-principles phonon calculations in materials science, *Scr. Mater.*, 2015, **108**, 1–5, DOI: 10.1016/j.scriptamat.2015.07.021.

56 V. Wang, N. Xu, J. C. Liu, G. Tang and W. T. Geng, VASPKIT: A user-friendly interface facilitating high-throughput computing and analysis using VASP code, *Comput. Phys. Commun.*, 2021, **267**, 108033, DOI: 10.1016/j.cpc.2021.108033.

57 T. Ouahrani, R. Khenata, B. Lasri, A. H. Reshak, A. Bouhemadou and S. Bin-Omran, First and second harmonic generation of the $XAl_2Se_4$ (X = Zn, Cd, Hg) defect chalcopyrite compounds, *Phys. B: Condens. Matter*, 2012, **407**, 3760–3766, DOI: 10.1016/j.physb.2012.05.057.

58 S. Belarouci, T. Ouahrani, N. Benabdallah and Á. Morales-García, Two-dimensional silicon carbide structure under uniaxial strains, electronic and bonding analysis, *Comput. Mater. Sci.*, 2018, **151**, 288–295, DOI: 10.1016/j.commatsci.2018.05.020.

59 L. Hedin, New Method for Calculating the One-Particle Green's Function with Application to the Electron-Gas Problem, *Phys. Rev.*, 1965, **139**, A796, DOI: 10.1103/PhysRev.139.A796.

60 M. S. Hybertsen and S. G. Louie, Electron correlation in semiconductors and insulators: Band gaps and quasiparticle energies, *Phys. Rev. B: Condens. Matter Mater. Phys.*, 1986, **34**, 5390, DOI: 10.1103/PhysRevB.34.5390.

61 R. M. Boufatah, T. Ouahrani and M. Benaissa, Electronic and optical properties of wolframite-type $ScNbO_4$: the effect of the rare-earth doping, *Eur. Phys. J. B*, 2022, **95**, 166, DOI: 10.1140/epjb/s10051-022-00427-5.

62 E. E. Salpeter and H. A. Bethe, A relativistic equation for bound-state problems, *Phys. Rev.*, 1951, **84**, 1232–1242, DOI: 10.1103/PhysRev.84.1232.

63 S. M. Dancoff, Non-Adiabatic Meson Theory of Nuclear Forces, *Phys. Rev.*, 1950, **78**, 382, DOI: 10.1103/PhysRev.78.382.

64 F. Aryasetiawan and O. Gunnarsson, The GW method, *Rep. Prog. Phys.*, 1998, **61**, 237–312, DOI: 10.1088/0034-4885/61/3/002.

65 W. G. Aulbur, L. Jönsson and J. W. Wilkins, Quasiparticle calculations in solids, *J. Phys. C: Solid State Phys.*, 2000, **54**, 1–218, DOI: 10.1016/S0081-1947(08)60248-9.

66 S. L. Adler, Quantum theory of the dielectric constant in real solids, *Phys. Rev.*, 1962, **126**, 413–420, DOI: 10.1103/PhysRev.126.413.

67 N. Wiser, Dielectric constant with local field effects included, *Phys. Rev.*, 1963, **129**, 62–69, DOI: 10.1103/PhysRev.129.62.

68 H. Ehrenreich and M. H. Cohen, Self-consistent field approach to the many-electron problem, *Phys. Rev.*, 1959, **115**, 786–790, DOI: 10.1103/PhysRev.115.786.

69 R. I. Eglitis and D. Vanderbilt, Ab initio calculations of $BaTiO_3$ and $PbTiO_3$ (001) and (011) surface structures, *Phys. Rev. B: Condens. Matter Mater. Phys.*, 2007, **76**, 155439, DOI: 10.1103/PhysRevB.76.155439.

70 H. Qiu, T. Yang, J. Zhou, K. Yang, Y. Ying, K. Ding, M. Yang and H. Huang, Tunable hydrogen evolution activity by modulating polarization states of ferroelectric $BaTiO_3$, *J. Mater. Chem. A*, 2023, **11**, 7034, DOI: 10.1039/d2ta07907k.

71 B. Meyer, J. Padilla and D. Vanderbilt, Theory of $PbTiO_3$, $BaTiO_3$, and $SrTiO_3$ Surfaces, *Faraday Discuss.*, 1999, **114**, 395–405, DOI: 10.1039/A903029H.

72 J. K. Nørskov, J. Rossmeisl, A. Logadottir, L. Lindqvist, J. R. Kitchin, T. Bligaard and H. Jonsson, Origin of the Overpotential for Oxygen Reduction at a Fuel-Cell

Cathode, *J. Phys. Chem. B*, 2004, **108**, 17886–17892, DOI: 10.1021/jp047349j.

73 A. Bouheddadj, A. Daouli, T. Ouahrani, R. M. Boufatah and M. Badawi, Unveiling the electronic properties of the Janus HfSSe monolayer and its partially oxygenated counterparts from ab initio calculations, *Mater. Chem. Phys.*, 2022, **289**, 126489, DOI: 10.1016/j.matchemphys.2022.126489.

74 X. Gonze and C. Lee, Dynamical matrices, Born effective charges, dielectric permittivity tensors, and interatomic force constants from density-functional perturbation theory, *Phys. Rev. B: Condens. Matter Mater. Phys.*, 1997, **55**, 10355, DOI: 10.1103/PhysRevB.55.10355.

75 A. Togo and I. Tanaka, First-principles phonon calculations in materials science, *Scr. Mater.*, 2015, **108**, 1–5, DOI: 10.1016/j.scriptamat.2015.07.021.

76 Z. Li, M. Grimsditch, X. Xu and S.-K. Chan, The elastic, piezoelectric and dielectric constants of tetragonal $PbTiO_3$ single crystals, *Ferroelectrics*, 1993, **141**, 313–325, DOI: 10.1080/00150199308223459.

77 J. A. Brehm, H. Takenaka, C. W. Lee, I. Grinberg, J. W. Bennett, M. R. Schoenberg and A. M. Rapp, Density functional theory study of hypothetical $PbTiO_3$-based oxysulfides, *Phys. Rev. B: Condens. Matter Mater. Phys.*, 2014, **89**, 195202, DOI: 10.1103/PhysRevB.89.195202.

78 A. G. Kalinichev, J. D. Bass, B. N. Sun and D. A. Payne, Elastic properties of tetragonal $PbTiO_3$ single crystals by Brillouin scattering, *J. Mater. Res.*, 1997, **12**, 2623–2627, DOI: 10.1557/JMR.1997.0349.

79 Z. Wu and R. E. Cohen, Pressure-Induced Anomalous Phase Transitions and, Colossal Enhancement of Piezoelectricity in $PbTiO_3$, *Phys. Rev. Lett.*, 2005, **95**, 037601, DOI: 10.1103/PhysRevLett.95.037601.

80 Y. Liu, G. Xu, C. Song, Z. Ren, G. Han and Y. Zheng, First-principles study of elastic properties in perovskite $PbTiO_3$, *Mater. Sci. Eng., A*, 2008, **472**, 269–272, DOI: 10.1016/j.msea.2007.03.028.

81 J. Singh, S. S. Sahoo, K. Venkatakrishnan, G. Vaitheeswaran and D. Errandonea, High-pressure study of the aurophilic topological Dirac material, AuI, *J. Alloys Compd.*, 2022, **928**, 167178, DOI: 10.1016/j.jallcom.2022.167178.

82 K. Choudhary, K. F. Garrity, A. C. E. Reid, B. DeCost, A. J. Biacchi, A. R. Hight Walker, Z. Trautt, J. Hattrick-Simpers, A. G. Kusne, A. Centrone, A. Davydov, J. Jiang, R. Pachter, G. Cheon, E. Reed, A. Agrawal, X. Qian, V. Sharma, H. Zhuang, S. V. Kalinin, B. G. Sumpter, G. Pilania, P. Acar, S. Mandal, K. Haule, D. Vanderbilt, K. Rabe and F. Tavazza, The joint automated repository for various integrated simulations (JARVIS) for data-driven materials design, *npj Comput. Mater.*, 2020, **6**, 173, DOI: 10.1038/s41524-020-00440-1.

83 E. Ching-Prado, A. Reynés-Figueroa, R. S. Katiyar, S. B. Majumder and D. C. Agrawal, Raman spectroscopy and, X-ray diffraction of $PbTiO_3$ thin film, *J. Appl. Phys.*, 1995, **78**, 1920–1925, DOI: 10.1063/1.360229.

84 D. Errandonea, A. Muñoz, P. Rodríguez-Hernández, O. Gomis, S. N. Achary, C. Popescu, S. J. Patwe and A. K. Tyagi, High-Pressure Crystal Structure, Lattice Vibrations, and Band Structure of $BiSbO_4$, *Inorg. Chem.*, 2016, **55**(10), 4958–4969, DOI: 10.1021/acs.inorgchem.6b00503.

85 O. Gomis, R. Vilaplana, F. J. Manjón, D. Santamaría-Pérez, D. Errandonea, *et al.* High-pressure study of the structural and elastic properties of defect chalcopyrite $HgGa_2Se_4$, *J. Appl. Phys.*, 2013, **113**, 073510, DOI: 10.1063/1.4792495.

86 T. Ouahrani, A. Otero-de-la-Roza, R. Khenata, V. Luaña and B. Amrani, Structural and thermodynamic properties of SbAsGa2 and $SbPGa_2$ chalcopyrites, *Comput. Mater. Sci.*, 2009, **47**, 655–659, DOI: 10.1016/j.commatsci.2009.10.001.

87 M. Ali, A. Khan, S.-H. Khan, T. Ouahrani, G. Murtaza, R. Khenata and S.-B. Omran, First-principles study of Cu based delafossite transparent conducting oxides $CuXO_2$ (X = Al, Ga, In, B, La, Sc, Y), *Mater. Sci. Semicond. Process.*, 2015, **38**, 57–66, DOI: 10.1016/j.mssp.2015.03.038.

88 T. Ouahrani, R. Khenata, B. Lasri, A. H. Reshak, A. Bouhemadou and S. Bin-Omran, First and second harmonic generation of the $XAl_2Se_4$ (X = Zn, Cd, Hg) defect chalcopyrite compounds, *Phys. B: Condens. Matter*, 2012, **407**, 3760–3766, DOI: 10.1016/j.physb.2012.05.057.

89 W. Voigt, *Lehrbuch der Kristallphysik*, Teubner Verlag, Leipzig, 1928.

90 A. Reuss, Berechnung der Fliessgrenze von Mischkristallen auf Grund der Plastizitätsbedingung für Einkristalle. ZAMM—Journal of Applied Mathematics and Mechanics/Zeitschrift für Angewandte Mathematik und Mechanik, *Z. Angew. Math. Mech.*, 1929, **9**, 49–58, DOI: 10.1002/zamm.19290090104.

91 R. Hill, The Elastic Behaviour of a Crystalline Aggregate, *Proc. Phys. Soc., Sect. A*, 1952, **65**, 349–354, DOI: 10.1088/0370-1298/65/5/307.

92 S. F. Pugh, Relations between the elastic moduli and the plastic properties of polycrystalline pure Metals, *Philos. Mag. A*, 1954, **45**, 823–843, DOI: 10.1080/14786440808520496.

93 O. Gomis, B. Lavina, P. Rodríguez-Hernández, A. Muñoz, R. Errandonea, D. Errandonea and M. Bettinelli, High-pressure structural, elastic, and thermodynamic properties of zircon-type $HoPO_4$ and $TmPO_4$, *J. Phys.: Condens. Matter*, 2017, **29**, 095401, DOI: 10.1088/1361-648X/aa516a.

94 E. M. Hutter, M. C. Gélvez-Rueda, A. Osherov, V. Bulovi, F. C. Grozema, S. D. Stranks and T. J. Savenije, Direct-indirect character of the bandgap in methylammonium lead iodide perovskite, *Nat. Mater.*, 2017, **16**, 115, DOI: 10.1038/nmat4765.

95 P. h. Ghosez, E. Cockayne, U. V. Waghmare and K. M. Rabe, Lattice dynamics of BaTiO3, $PbTiO_3$, and PbZrO3:A comparative first-principles study, *Phys. Rev. B: Condens. Matter Mater. Phys.*, 1999, **60**, 836, DOI: 10.1103/PhysRevB.60.836.

96 P. Ganesh and R. E. Cohen, Pressure-induced phase transitions in $PbTiO_3$, *J. Phys.: Condens. Matter*, 2009, **21**, 064225, DOI: 10.1088/0953-8984/21/6/064225.

97 M. Ahart, M. Somayazulu, R. E. Cohen, P. Ganesh, P. Dera, H.-K. Mao, R. J. Hemley, Y. Ren, P. Liermann and Z. Wu, Origin of morphotropic phase boundaries in ferroelectrics, *Nature*, 2008, **451**, 545–548, DOI: **10.1038/nature06459**.

98 F. Bassani, G. P. Parravicini and R. A. Ballinger (ed.), J. L. Birman (Reviewer), Electronic States and optical transitions in solids, *Phys. Today*, 1976, 29, 58. DOI: **10.1063/1.3023374**.

99 M. Fox and G. F. Bertsch, Optical properties of solids, *Am. J. Phys.*, 2002, **70**, 1269, DOI: **10.1119/1.1691372**.

100 P. Liu, B. Kim, X.-Q. Chen, D. D. Sarma, G. Kresse and C. Franchini, Relativistic GW + BSE study of the optical properties of Ruddlesden-Popper iridates, *Phys. Rev. Mater.*, 2018, **2**, 075003, DOI: **10.1103/PhysRevMaterials.2.075003**.

101 R. Su, Z. P. Wang, L. N. Zhu, Y. Pan, D. W. Zhang, H. Wen, Z. D. Luo, L. L. Li, F. T. Li, M. Wu, L. Q. He, P. Sharma and J. Seidel, *Angew. Chem., Int. Ed.*, 2021, **60**, 16019–16026, DOI: **10.1002/anie.202103112**.

102 T. Ouahrani, R. M. Boufatah, M. Benaissa, Á.Á Morales-García, M. Badawi and D. Errandonea, Effect of intrinsic point defects on the catalytic and electronic properties of $Cu_2WS_4$ single layer: Ab initio calculations, *Phys. Rev. Mater.*, 2023, **7**, 025403, DOI: **10.1103/PhysRevMaterials.7.025403**.

103 T. Ouahrani, A. Daouli, M. Badawi, L. Bendaoudi, A. Á Morales-García and D. Errandonea, Understanding the thermodynamic, dynamic, bonding, and electrocatalytic properties of low dimensional $MgPSe_3$, *Dalton Trans.*, 2022, **51**, 9689–9698, DOI: **10.1039/D2DT01194H**.

104 C. He, G. Liu, H. Zhao, K. Zhao, Z. Ma and X. An, Inorganic photovoltaic cells based on $BiFeO_3$: spontaneous polarization, lattice matching, light polarization and their relationship with photovoltaic performance, *Phys. Chem. Chem. Phys.*, 2020, **22**, 8658–8666, DOI: **10.1039/D0CP01176B**.